Snow Water Equivalent Retrieval Over Idaho, Part A: Using Sentinel-1 Repeat-Pass Interferometry

Shadi Oveisgharan[1], Robert Zinke[1], Zachary Hoppinen[2], and Hans Peter Marshall[2]

[1]Jet Propulsion Laboratory, California Institute of Technology, 4800 Oak Grove Dr, Pasadena, CA, USA
[2]Boise State University, Department of Geosciences, 1295 University Drive, Boise, ID, USA

Correspondence: Shadi Oveisgharan (Shadi.Oveisgharan@jpl.nasa.gov)

Abstract. Snow Water Equivalent (SWE) is identified as the key element of the snowpack that impacts rivers' streamflow and water cycle. Both active and passive microwave remote sensing methods have been used to retrieve SWE, but there does not currently exist a SWE product that provides useful estimates in mountainous terrain. Active sensors provide higher-resolution observations, but the optimal radar frequencies and temporal repeat intervals have not been available until recently.

5   Interferometric Synthetic Aperture Radar (InSAR) has been shown to have the potential to estimate SWE change. In this study, we apply this technique to a long time series of Sentinel-1 data from the 2020-2021 winter. The retrievals show statistically significant correlations both temporally and spatially with independent measurements of snow depth and SWE. The Pearson correlation and RSME between retrieved SWE change observations and in situ stations measurements are 0.82, and 0.76cm, respectively. The total retrieved SWE in the entire 2020-2021 time series shows SWE error less than 2cm for the 16 in situ

10   stations in the scene. Additionally, the retrieved SWE using Sentinel-1 data is highly correlated with LIDAR snow depth data with correlation of more than 0.5. Low temporal coherence is identified as the main reason for degrading the performance of SWE retrieval using InSAR data. Low temporal coherence also causes the degradation of phase unwrapping algorithms.

1 Introduction

The seasonal snowpack provides water resources to billions of people worldwide (Barnett et al., 2005). Snow is the primary

15   source of water for river channel discharge in middle-to-high latitude areas. Therefore, snow cover has a great impact on global and regional water cycles. Large scale mapping of snow water equivalent (SWE) with high resolution is critical for many scientific and economics fields. SWE is defined as the depth of water which would be obtained if all ice contained in the snow pack were melted. NASA SnowEx is a multi-year effort to improve SWE and snow surface energy balance measurements and estimates. SWE has been identified as the key variable for terrestrial snow by the SnowEx campaign and NASA's decadal

20   survey.

Estimating SWE on a global scale with enough accuracy and resolution is still a challenge. Passive spaceborne sensors based on the microwave emission of the snow pack (Takala et al., 2011; Kelly et al., 2003; Pulliainen and Hallikainen, 2001; Kelly, 2009) have a coarse spatial resolution on the 10 kilometer-scale. The technique saturates for SWE deeper than 150mm, which makes their application in the mountains challenging. Nevertheless, passive microwave sensors represent the current state-of-

25   the-art of SWE retrieval methods. These sensors are applied operationally to generate daily estimates of SWE globally (Takala et al., 2011; Kelly et al., 2003), however many products such as GlobSnow mask out mountainous areas, due to the saturation limit and resolution.

Airborne LIDAR has been successful in estimating snow depth (Painter and et al., 2016). However, clouds and limited regional coverage are limiting factors for this method. This technique also needs a snow density model to estimate SWE from

30   the LIDAR snow depth , and there currently is not a path to space for global snow depth mapping at the temporal resolution required.

Active microwave sensors provide high resolution and global coverage. SWE can be retrieved using active microwave remote sensing from space (Cui et al., 2016; Leinss et al., 2014, 2015; Oveisgharan and Zebker, 2007; Lemmetyinen et al., 2018; Yueh et al., 2017, 2021; Conde et al., 2019; Liu et al., 2017; Eppler et al., 2022; Dagurova et al., 2020; Nagler et al.,

35   2022; Engen et al., 2004; Larsen et al., 2005; Lievens et al., 2019). Backscattered power from active sensors can be used to estimate SWE (Rott et al., 2010; Ulaby and Stiles, 1980; Cui et al., 2016; Nghiem and Tsai, 2001; Lievens et al., 2019). A correlation of 0.97 with a change of 108 mm per dB was observed between QuickSCAT backscattered power and SWE for SWE of less than 200 mm (Nghiem and Tsai, 2001). A dual-band (X and Ku) SAR mission has been the focus of the European Space Agency (ESA) and Canadian Space Agency (CSA) for SWE spaceborne measurements (Rott et al., 2010; Lemmetyinen

40   et al., 2018). However, accurate *a priori* characterization of snow micro-structural parameters is of primary importance in the accuracy of SWE retrieval algorithms using backscattered power (Lemmetyinen et al., 2018; Durand and Liu, 2012; Cui et al., 2016). The most common *a priori* characterization used for SWE retrieval algorithms using backscattered power is grain radius. This has been done using passive data; however, the methods are restricted to passive retrieval errors and also mismatch between active and passive resolutions. The ratio of cross-pol to co-pol Sentinel-1 backscattered power has been

45   used to estimate snow depth over mountainous regions with deep snow (Lievens et al., 2019, 2022), however the radiative transfer physics at C-band are still poorly understood.

Lightweight and portable Frequency Modulated Continuous Wave (FMCW) radar systems have been used to map snow pack properties (such as depth, SWE, and stratigraphy) rapidly over large distances and at high resolution (Marshall and Koh, 2008). However, these sensors cannot be used in spaceborne missions for global coverage due to their wide bandwidth.

50   The phase change of specularly reflected signals from the snow-ground interface has been shown to be strongly dependent on SWE changes for dry snow (Leinss et al., 2015; Guneriussen et al., 2001; Ruiz et al., 2022) ; in wet snow the phase center is normally at the snow surface, and the phase change is related to depth changes (Yueh et al., 2017, 2021; Shah et al., 2017). The phase sensitivity to SWE changes increases at higher frequencies. However, the phase unwrapping and loss of coherence increase at higher frequencies. The theory behind this method is similar to repeat pass interferometry that is explained in section

55   2. The advantage of this method is that the stratigraphy of the snow has little impact on the SWE retrieval using this method (Yueh et al., 2017), and information about snow microstructure is not needed.

As explained in details in next section, the phase difference between two SAR observations is proportional to small changes in SWE variation (ΔSWE). We evaluated the performance of SWE retrieval using interferometry over Idaho. In part (A) of this study (the current paper), we used Sentinel-1 interferometric time series data over Idaho. In part (b), we will use Uninhabited

60   Aerial Vehicle Synthetic Aperture Radar (UAVSAR) interferometric time series data over Idaho to evaluate the performance of
this method. We explain this retrieval method in section 2. The details about different data sets used in this study are discussed
in section 3. Section 4 describes how we processed Sentinel-1 data and convert it to SWE. The retrieved SWE is compared
with in situ and LIDAR data in section 5. This work shows for the first time the success of SWE retrieval using a long time
series spaceborne InSAR data.

2   Using Differential Interferometry to Estimate SWE

Differential SAR interferometry measurements have been used to detect small surface elevation changes over large areas with a
vertical accuracy of a few millimeters (Gabriel et al., 1989; Zebker et al., 1994). The measured phase difference is proportional
and very sensitive to small changes in SWE variation (ΔSWE) during the snow season (Guneriussen et al., 2001; H. Rott and
Scheiber, 2003; Deeb et al., 2011; Leinss et al., 2015; Conde et al., 2019; Liu et al., 2017; Hui et al., 2016; Nagler et al., 2022;
70   Eppler et al., 2022; Dagurova et al., 2020; Marshall et al., 2021). The main advantage of this method is its simplicity and a
reduction in necessary *a priori* information.

    The snow volume scattering affects the interferometric phase for very deep snow in Greenland at higher frequencies such
as C-band (Oveisgharan and Zebker, 2007). However, for the terrestrial snow, the effect of volume scattering of dry snow
on the interferometric phase is very small compared to scattering from the ground at high frequencies. The snow refractive
75   index delays the echo received from the ground. The signal delay caused by refraction can be measured with differential radar
interferometry as (Guneriussen et al., 2001; Leinss et al., 2015):

$$\Delta\phi = -2\kappa_i(\cos\theta - \sqrt{\epsilon - \sin^2\theta})\Delta d \tag{1}$$

where $\Delta\phi, \kappa_i, \Delta d, \theta$, and ϵ are interferometric phase between two observation dates, incidence wavenumber, snow depth
change, incidence angle, and permittivity of the snow, respectively. The change in interferometric phase is used to calcu-
80   late ΔSWE (Leinss et al., 2015; Conde et al., 2019; Liu et al., 2017; Nagler et al., 2022). Similar to the dual-pol. dual-freq.
retrieval algorithm, this technique relies on the dryness of snow in order to penetrate all the way to the ground.

    Using Envisat interferometric data to estimate SWE was not very successful mainly due to large temporal baseline and,
hence, low temporal coherence (Hui et al., 2016). A modified version of SWE estimation using InSAR is also introduced
(Eppler et al., 2022; Dagurova et al., 2020). The backscattering from the roughness in the ground and snow layers are combined
85   with interferometric phase to improve the accuracy (Dagurova et al., 2020). The sensitivity of the dry-snow refraction-induced
InSAR phase to topographic variations is used to bypass the unwrapping problem (Eppler et al., 2022). Airborne data collected
over the Austrian Alps in 2021 showed good agreement between retrieved SWE using InSAR and mean in situ SWE. Root-
mean-square difference of 4.0 mm for a small snow storm of 14mm snow depth at C-band and 11.2mm for a big snow
storm of 66mm at L-band were observed (Nagler et al., 2022). The retrieved SWE change using L-band UAVSAR differential
90   interferometry between 2/1/2020 and 2/13/2020 was highly correlated with the collected LIDAR snow depth change between
2/1/2020 and 2/12/2020 over the open regions of Grand Mesa in dry snow conditions (Marshall et al., 2021). SWE retrieval

using Sentinel-1 interferometric data showed mean accuracy of 6mm over Finland for just two passes (Conde et al., 2019). All these studies have proven the potential of this method but were limited in time or space for data collection or validation. In this study, we show the performance of SWE retrieval using a long time series of Sentinel-1 interferometric data in winter 2021.

95   This study shows for the first time that SWE estimation using repeat pass interferometry works well by validating the retrieved value with a large number of in situ stations and two regional LIDAR snow depth maps.

With the recent SnowEx 2020 campaign using UAVSAR L-band differential interferometry data, Sentinel-1 C-band differential interferometry, and future NASA-ISRO SAR (NISAR) L-band data, there will be more advances in the limitations and capabilities of this method.

100   2.1   Temporal Coherence

The received radar signals at two different days will be correlated with each other if the set of scatterers in the resolution cell remain the same. However, the scatterers such as leaves and branches in vegetated areas move and decrease the temporal coherence (Zebker and Villasenor, 1992; Kellndorfer et al., 2022; Lavalle et al., 2012). The loss of coherence between the observations is one of the main limitations for SWE retrieval using differential interferometry. Methods such as using two

105   frequencies or faster sampling are used to overcome these problems (Deeb et al., 2011; Leinss et al., 2015). Melting and wind are the main reasons for low temporal coherence in snow (Leinss et al., 2015; Luzi et al., 2009). A high temporal coherence is observed at L-band for dry snow with a month temporal baseline (Molan et al., 2018). Temporal coherence decreases with increasing frequency (Leinss et al., 2015; Nagler et al., 2022; Kellndorfer et al., 2022; Ruiz et al., 2022). A median temporal coherence of about 0.5 is observed at 10.2 GHz and 16.8 GHz even after 60 days (Leinss et al., 2015) for a controlled system.

110   However, the spaceborne TerraSAR-X temporal coherence over snow at 9.65 GHz reduces significantly in 11 days (Leinss et al., 2014). This is probably due to random phase drifts over time that cannot be estimated and corrected in a spaceborne system compared to a ground radar. Vegetation cover decreases the temporal coherence significantly at high frequencies (Baduge et al., 2016; Kellndorfer et al., 2022; Ruiz et al., 2022). A tower-based fully polarimetric InSAR studied the effect of air temperature, precipitation intensity, and wind on the temporal decorrelation at L-, S-, C-, and X-bands (Ruiz et al., 2022). The temperature

115   was shown to be the most critical variable affecting the temporal coherence among other variables. SWE accumulation profile retrieval was successful for short temporal baselines and low frequencies in non-vegetated areas. However, the error increased for high frequencies and long temporal baselines. The SWE profile retrieval using C-band data performs well using 12 hours and 1 day repeat-pass data. The retrieval is poor using the 12-day repeat-pass data at C-band (Ruiz et al., 2022). 6-day repeat pass C-band data showed good performance for small SWE changes but poor performance for large SWE changes between

120   the interferometric pairs due to phase ambiguity caused by large SWE change (Ruiz et al., 2022). More studies are needed to better model temporal coherence at different frequencies, different land types, and different environmental conditions. The low temporal coherence and low penetration depth at frequencies higher than 10 GHz, make L- and C-band desirable frequencies for differential interferometry.

2.2 Relationship between ΔSWE and $\Delta\phi$

125 With some approximation to equation 1, Leinss et al. related the interferometric phase directly to SWE change (Leinss et al., 2015). The approximation depends on the range of incidence angles and snow density. Here we try to make a more genaralized approximation. The snow permittivity in equation 1 is dependent on snow density, ρ, and relatively independent of signal wavelength. We use Matzler's model for calculating ϵ in equation 1 (Mätzler, 1987). We can rewrite equation 1 as

$$\Delta\phi = -2\kappa_i C(\theta,\rho)\Delta SWE \tag{2}$$

130 where $C(\theta,\rho) = \frac{1}{\rho}(\cos\theta - \sqrt{\epsilon(\rho) - \sin^2\theta})$
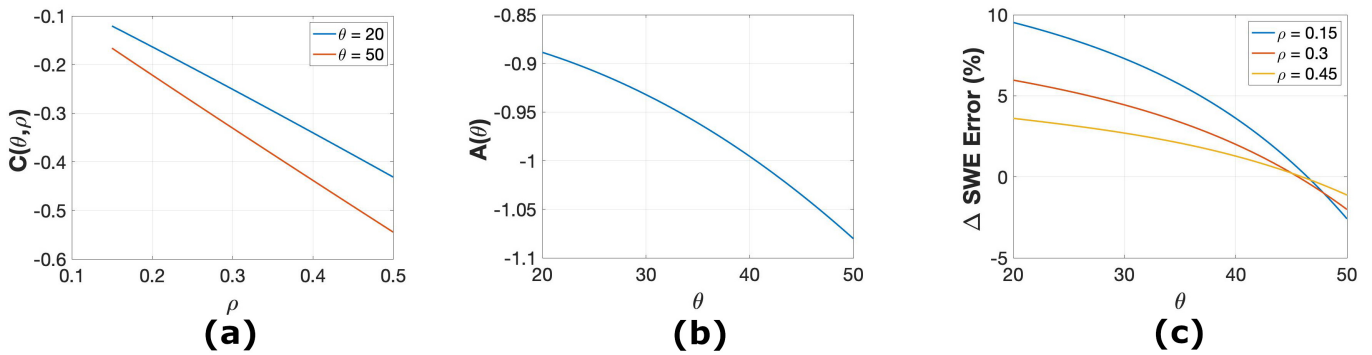

Figure 1. (a) $C(\theta,\rho)$ versus snow density for $\theta = 20$ and $\theta = 50$ shown by blue and red lines, respectively (b) The line slope in part (a) versus incidence angle (c) ΔSWE error percentage assuming $C = A\rho$ versus incidence angle for snow density equal to 0.15, 0.3, and 0.45 g/cm^3, shown by blue, red, and yellow lines, respectively.

The blue and red lines in figure 1 (a) show $C(\theta,\rho)$ versus snow density for incidence angles equal to 20 and 50 degrees, respectively. As seen in this figure, there is approximately a linear relationship between C and snow density. We fit a line to C for different incidence angles as $C(\theta,\rho) = A(\theta) \times \rho + B(\theta)$. Figure 1 (b) shows $A(\theta)$ versus incidence angle. By fitting a polynomial to A, we can write it as

135 $$A = -0.3385\theta^2 + 0.0486\theta - 0.8647 \tag{3}$$

As seen in figure 1(a), B is very close to zero. Assuming $B(\theta) = 0$, we can rewrite the equation 1 as

$$\Delta\phi = -2\kappa_i(-0.3385\theta^2 + 0.0486\theta - 0.8647)\Delta S\hat{W}E \tag{4}$$

Figure 1(c) shows the $\frac{\Delta SWE - \Delta S\hat{W}E}{\Delta SWE} \times 100$ versus incidence angle for different snow densities. As seen in this figure, the error in ΔSWE calculation using the approximation in equation 4 is less than 10%. We use equation 4 for estimating ΔSWE
140 using interferometric phase, $\Delta\phi$, for the rest of this study.

3 Datasets

3.1 Sentinel-1

The Sentinel-1 radar operates at C-band. It has four exclusive imaging modes with different resolutions (down to 5 m) and swath width up to 400 km. Sentinel-1 has dual polarization capability, short revisit times (12 days), and rapid product delivery.
145 The data are free and available through Alaska SAR Facility (ASF). The vv and vh (transmit-received polarization) differential interferometric phase and coherence can be generated using ASF On Demand Processing globally every 12 days. Alaska Satellite Facility's Hybrid Pluggable Processing Pipeline (HyP3) is a service for processing Synthetic Aperture Radar (SAR) imagery. The workflow includes interferometric phase correction for ground topography and geolocation. The ASF HYP3 uses a Minimum Cost Flow (MCF) algorithm for phase unwrapping. The unwrapped phase and interferometric correlation were
150 used in this study. Sentinel-1 collects data every 12 days globally but has the capability to collect the data every 6 days over targeted areas, mainly over Europe.
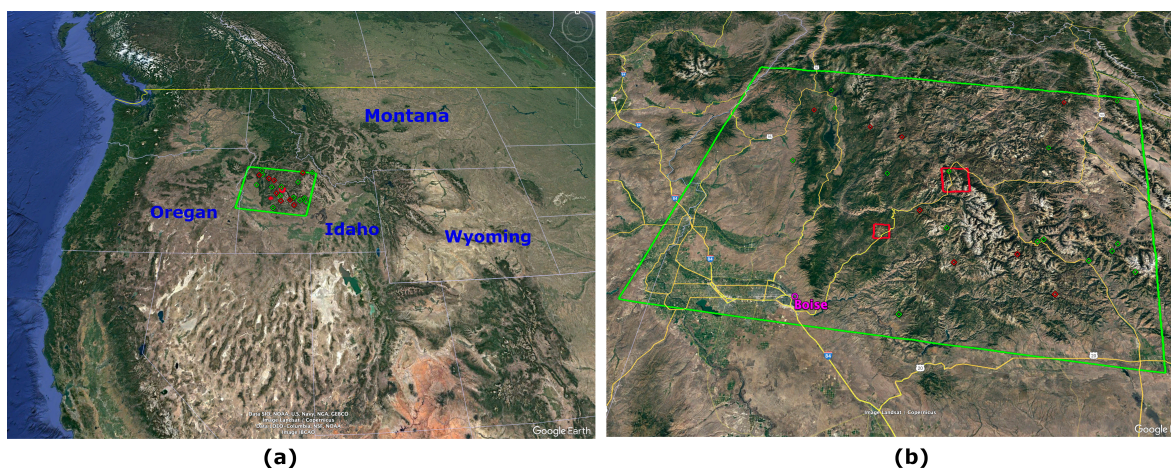

Figure 2. © Google Earth View (a) Google Earth View of Sentinel-1 path:71, frame:444 in Idaho. Red boxes show the location of LIDAR data acquisition. (b) zoomed to the Sentinel-1 path:71, frame:444

The NASA SnowEx2021 Time Series is the continuation of the multi-year effort to improve SWE measurements and estimates. The data acquisition for different sensors and in situ collections spread over different US sites in winter 2020. These sites span a range of snow climates and conditions, elevations, aspects, and vegetation. Flight paths were designed to include
155 sites with ongoing snow research projects, existing ground-based remote sensing infrastructure (e.g., radar and LIDAR), snow-off and planned snow-on aerial LIDAR, and scheduled ground snow measurement. The 2021 Time Series data set covers fewer regional sites and more frequent temporal sampling compared to the 2020 campaign. The SnowEx campaign coordinated with Sentinel-1 team to observe some of the SnowEx sites with 6 days revisit during the winter, which included the Idaho SnowEx sites.

6

The Cryosphere
Discussions

160 Figure 2(a) shows one of these sites that was observed every 6 days with the Sentinel-1 over Idaho. The green frame shows the geographic location of path 71, frame 444 of Sentinel-1 data. Figure 2(b) is zoomed to the Sentinel-1 frame in part (a).
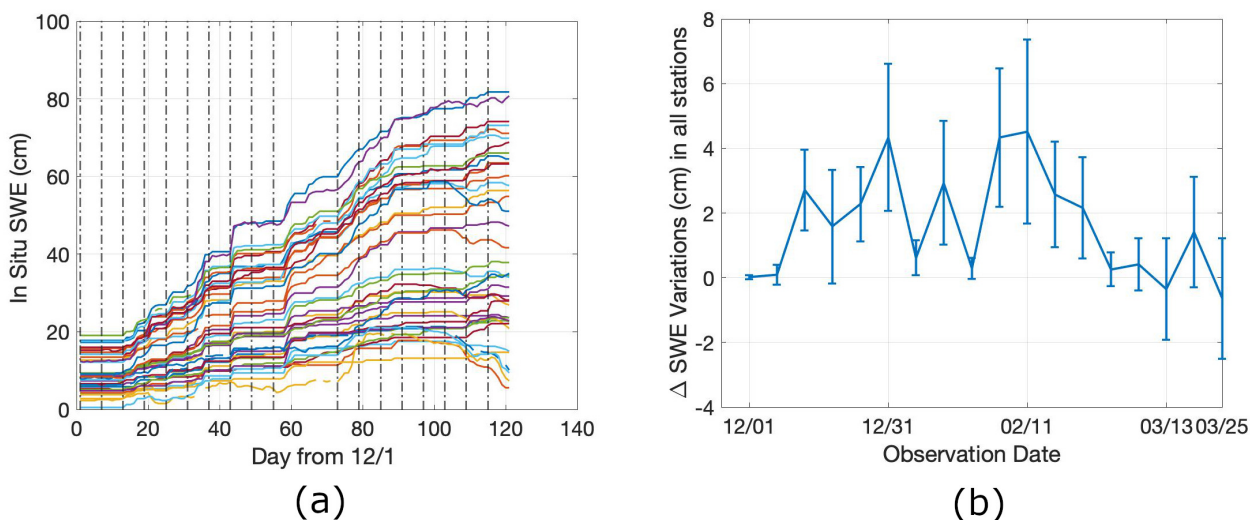
3.2 SNOTEL

Figure 3. (a) The daily SWE (cm) of in situ stations shown in figure 2(b) from 12/01/20 to 03/30/21. The dashed vertical lines show the start date of Sentinel-1 observations. (b) The mean $\pm$ std of in situ ΔSWE for Sentinel-1 observation dates shown in part (a).

SNOwpack TELemetry Network (SNOTEL) sites are located in remote, high elevated mountainous regions in the western US. They automatically measure different snowpack characteristics and climate conditions. We used the United States Depart-

165 ment of Agriculture (USDA) website to access hourly SNOTEL data (https://wcc.sc.egov.usda.gov/nwcc/inventory) over the region of interest shown in figure 2(b). As the Sentinel-1 frame in Idaho is collected at around 6 am local time, we downloaded the SWE, snow depth, and near surface air temperature at 6 am. Small red and green diamonds in figure 2(b) show the SNOTEL locations in Sentinel-1 frame. Figure 3 (a) shows the time series SWE of these SNOTEL sites starting from 12/1/2020 at 6am. Different colors show different SNOTEL locations. The dashed vertical lines are the start date of each 6-day repeat Sentinel-1

170 data. As seen in this figure, there is a one 6-day repeat data acquisition gap in Sentinel-1 data on 2/5/21. Figure 3 (b) shows the mean $\pm$ std of SNOTEL ΔSWE between the start date Sentinel-1 data in figure 3(a) and 6 days later. We used these in situ data for (a) SWE retrievals performance (as seen in section 5.1), and (b) the InSAR reference point (as explained in section 4).

3.3 QSI LIDAR

Airborne LIDAR provides high-resolution snow depth maps. These data are reliable sources of validation data, particularly a

175 powerful constraint for InSAR retrieval of SWE. The "SnowEx20-21 QSI LIDAR DEM 0.5m" data set is part of the SnowEx

2020 and SnowEx 2021 campaigns (Adebisi et al., 2022). The data includes digital elevation models, snow depth, and vegetation height with 5m spatial resolution. Data were acquired over multiple areas in Colorado, Idaho, and Utah during February 2020, March 2021, and September 2021. The two red boxes in figure 2(b) show the location of LIDAR data acquisition. The big red box is over Banner Summit and the small red box is over Mores Creek in Idaho. Figures 11(a) and 12(a) show the QSI snow depth over Barren Summit and Mores Creek, respectively. We used this data in section 5.2 to compare with retrieved SWE using Sentinel-1 data.

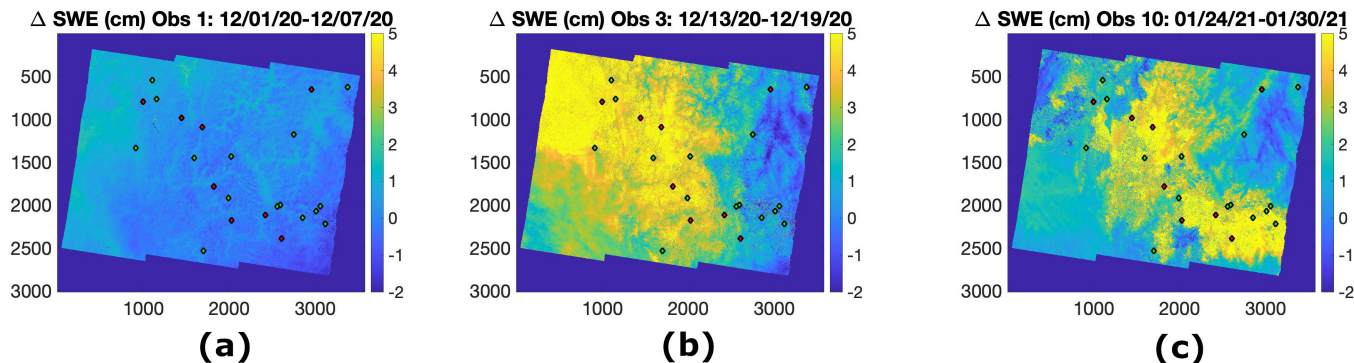## 4 SWE Retrieval Using Sentinel-1 interferometric Phase

Figure 4. Retrieved ΔSWE using Sentinel-1 path:71, frame:444 interferometric phase data between (a) 12/01/20 and 12/07/20 (b) 12/13/20 and 12/19/20 (c) 01/24/21 and 01/30/21. The small diamonds are in situ locations.

As mentioned in section 3.1, Sentinel-1 data were collected every 6 days over the region shown in figure 2(b) during 2020 and 2021, following coordination between the SnowEx campaign and the Sentinel-1 team. We used 6-day repeat Sentinel-1 time series data between 12/1/20 to 3/30/21. The main sources of error in the Sentinel-1 repeat-pass interferometry are (1) tropospheric noise, (2) temporal decorrelation, and (3) phase ambiguity. We removed tropospheric noise from the unwrapped phase as explained in section 4.1. The unwrapped phase is converted to ΔSWE using equation 4. Temporal decorrelation is relatively high at C-band. The 6-day repeat time improves the temporal coherence significantly over snow compared to the normal 12-day Sentinel-1 repeat time. In this study, any pixel with less than 0.35 temporal coherence is not considered reliable. Temporal coherence of 0.35 is arbitrary, but based on experience working with InSAR data, it is a reasonable threshold number. However, for the results in section 5.1.2 and 5.2, we used all the time series data, even with low coherence, to calculate total SWE. Phase ambiguity is still one of the big sources of error in some of our data as discussed in section 5.1.2. The ionospheric error at C-band is much smaller than other sources of error and we consider it negligible in this study.

The temperature is also an important factor. Equation 1 is valid for dry snow (Leinss et al., 2015), and we use near surface air temperature above zero as a metric that indicates wet snow. Any data with in situ near surface air temperature more than

zero is unreliable in our study. Similar to correlation filtering, for the results in section 5.1.2 and 5.2, we used all the time series data, even with temperature more than zero. However, above-zero temperatures were mostly observed by the end of March, so we can easily separate that effect.

200   Another important factor in interferometric phase images is the reference point to calibrate the unwrapped phase or consequently ΔSWE. In geophysics applications using InSAR, the reference point is a stable target with no displacement or known displacement in the time interval between acquisition of the two images. For ΔSWE estimation using InSAR, the reference point is chosen either by corner reflectors (cleaned of snow) with stable zero phase (Nagler et al., 2022; Dagurova et al., 2020) or using the average of in situ ΔSWE (Conde et al., 2019). As seen in figure 2(b), there are large number of in situ stations in this frame. This helps to reduce the effect of bias from specific stations. In this study, we used the average of all in situ ΔSWE

205   with reliable measurements (correlation more than 0.35 and temperature less than zero) to calibrate the retrieved ΔSWE images. Using the average of the subset of the in situ stations degrades our results in section 5 by less than 20%. So, we use average ΔSWE of all the in situ stations to improve our estimation in this study.

Figures 4(a), (b), and (c) show retrieved ΔSWE between 12/1/20 and 12/7/20, 12/13/20 and 12/19/20, and 1/24/21 and 1/30/21, respectively. The small squares show the location of in situ stations in this Sentinel-1 frame. The average of in situ

210   ΔSWE, for images 4(a), (b), and (c) are 0.01cm, 2.72 cm, and 4.33 cm, respectively. The retrieved ΔSWE images in figure 4 show no SWE change in part (a) and snow storms in part (b) and (c) which match the in situ measurements.
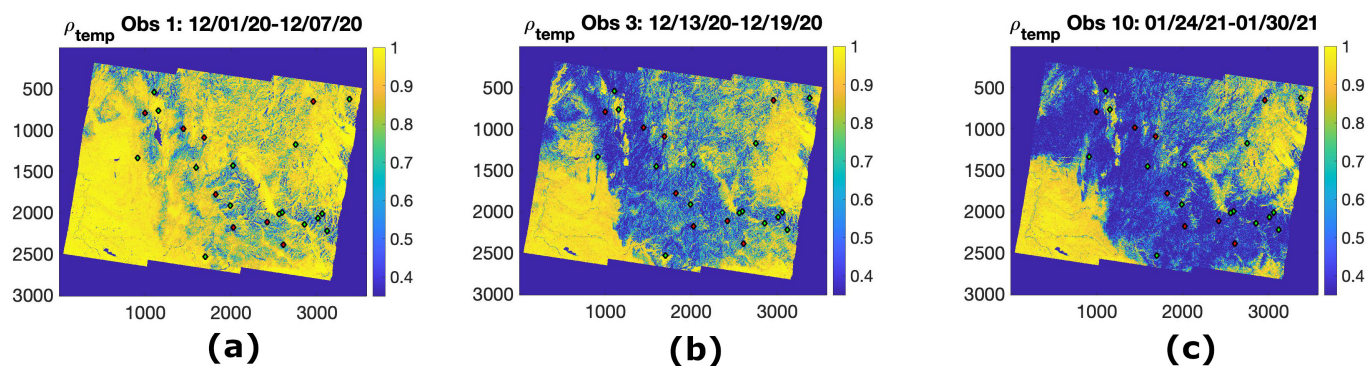

Figure 5. Sentinel-1 path:71, frame:444 correlation between (a) 12/01/20 and 12/07/20 (Observation 1) (b) 12/13/20 and 12/19/20 (Observation 3) (c) 01/24/21 and 01/30/21 (Observation 10).The small diamonds are in situ locations.

Figure 5 shows the temporal coherence of the images in 4. As shown in figures 5(b) and (c), snow storms reduce the correlation significantly whereas no SWE change shows very small decorrelation, as expected. Temporal coherence is one of the key limitations of retrieval using InsAR. Quantifying the optimum revisit time between two SAR images is one component

215   of our future work.

4.1 Tropospheric Noise Removal

A radio wave's differential phase delay variation through the troposphere is one of the largest error sources in Interferometric Synthetic Aperture Radar (InSAR) measurements, and water vapor variability in the troposphere is known to be the dominant factor. The differential delay present in a given interferogram may reach tens of centimeters. Various ways of mitigating tropospheric effects are routinely employed. Here, we used a global atmospheric weather model to predict the radar phase delay due to variations in atmospheric pressure and water vapor content. Specifically, we used the European Center for Medium-Range Weather Forecasts (ECMWF) ERA5 model of atmospheric variables, which provides hourly estimates on a 30 km global grid based on assimilation of surface and satellite meteorological data. We used the Python-based Atmospheric Phase Screen (PyAPS) software (Jolivet et al., 2011) to interpolate this grid, and convert those variables into a radar phase delay. PyAPS is integrated into, and leveraged by, the Miami InSAR Time-series software in Python (MintPy) (Yunjun et al., 2019). We used MintPy to crop the atmospheric delays to match the spatial extent of the interferograms, and projected the delays into radar line-of-sight (LOS). It should be noted that while the ERA weather models often provide a reliable method for representing atmospheric phenomena at $> 30 - km$ wavelengths (grid spacing), they are less accurate at finer spatial scale, where atmospheric conditions can vary as a function of topography. Model interpolation between grid nodes as a function of elevation were performed, however some over-smoothing of atmospheric variations might still occur. More work is necessary to better determine the overall effectiveness of atmospheric phase removal, including whether tropospheric delay is completely mitigated or over-corrected, and on what spatial scales.
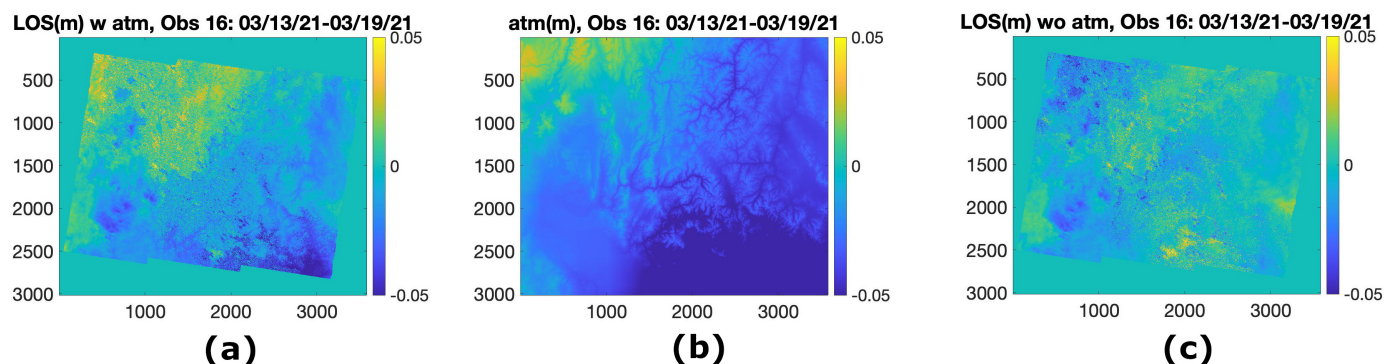

Figure 6. Sentinel-1 path:71, frame:444 (a) Line of Sight (LOS) displacement (m) With atmospheric noise (b) Atmospheric noise (m) (c) Line of Sight displacement (m) Without atmospheric noise, between 03/13/21 and 03/19/21.

Figure 6 shows an example of how significant tropospheric noise can be in an InSAR image. Figure 6(a) shows the line of sight (LOS) displacement with no atmospheric correction over our area of interest in figure 2(b) between 03/13/21 and 03/19/21. Figure 6(b) shows the atmospheric noise estimation using PyAPS. Figure 6(c) shows LOS displacement after tropospheric noise removal by subtracting 6(b) from 6(a). Comparing figures 6(a) and (c), we can see that the atmospheric noise can affect the estimated ΔSWE by 5-10cm (LOS displacement error converted to ΔSWE) in upper left of the images.

5 Results And Discussions

In this section we compare retrieved SWE using Sentinel-1 interferometric phase with in situ stations and LIDAR results.

5.1 Comparing Retrieved SWE using Sentinel-1 and SNOTEL SWE

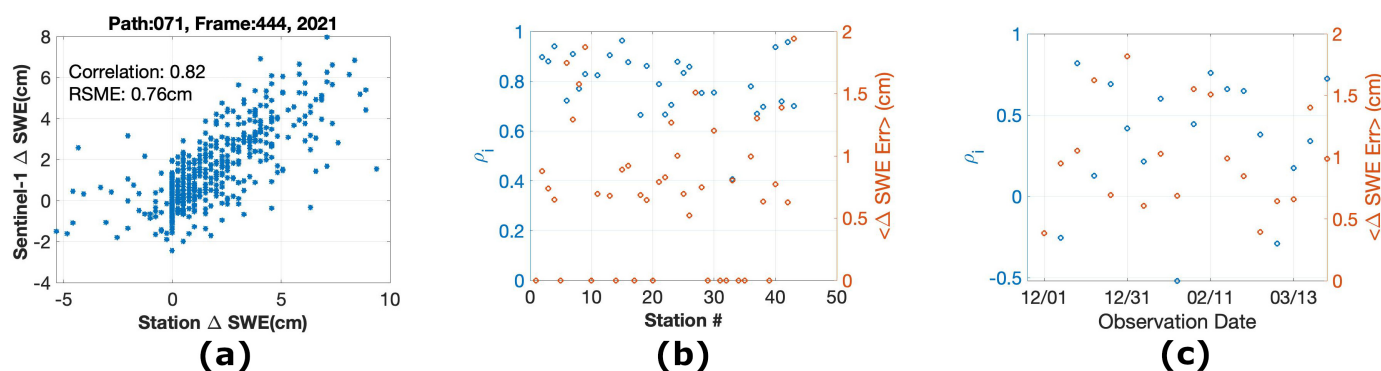#### 5.1.1 Comparing Retrieved ΔSWE using Sentinel-1 and SNOTEL ΔSWE

Figure 7. (a) Retrieved ΔSWE using Sentinel-1 interferometric phase and in situ ΔSWE for all the stations with temporal coherence more than 0.35 for the entire Sentinel-1 time series in 2020/2021. (b) Correlation (left axis) and absolute error (right axis) between retrieved ΔSWE using Sentinel-1 interferometric phase and in situ ΔSWE for each in situ station. (c) Correlation (left axis) and absolute error (right axis) between retrieved ΔSWE using Sentinel-1 interferometric phase and in situ ΔSWE for each interferogram.

We used all the retrieved ΔSWE (using the Sentinel-1 data from 12/1/20 to 3/30/21) for in situ stations shown in figure 2(b) and compared them with corresponding SNOTEL ΔSWE. As mentioned in section 4, any retrieved value with temporal coherence less than 0.35 and temperature higher than $0°C$ is discarded. Figure 7 (a) compares all the retrieved ΔSWE time series using Sentinel-1 data over all in situ stations with SNOTEL ΔSWE. As seen in this figure, the retrieved and in situ ΔSWE are highly correlated (0.82), with an RMSE of 0.76cm SWE.

Figure 7(b) shows the correlation and RSME between the entire time series of retrieved and in situ ΔSWE for each station, by blue and red circles respectively. As seen in this figure, the correlation is very good (more than 0.6 for all stations). The RSME is less than 2cm for all stations and less than 1cm for most stations.

Figure 7(c) shows the correlation and RSME between the in situ stations and retrieved ΔSWE for each Sentinel-1 acquisition first date, by blue and red circles respectively. The RSME is again less than 2cm for all dates and less than 1cm for many dates. As seen in this figure, the correlation is very good (more than 0.4) for some dates and poor (less than 0.4) for some others. Among the observation dates with correlation less than 0.35 (observation 1, 2, 4, 7, 15, 16, and 17), observations 1, 2, 7, 15, and 16 have very small snow accumulation (the average ΔSWE is less than 0.5cm). Therefore, the phase is not sensitive enough to SWE change, hence low correlation. For observation 4 and 17, we discovered that the low coherence degrades the

11

phase unwrapping performance for these InsAR images. Figure 8(a) and (b) show the wrapped phase for observations 4 and 5, respectively. Note that the correlation between in situ and retrieved ΔSWE in figure 7(c) is 0.1 for observation 4 and 0.7 for observation 5. The average in situ ΔSWE between 12/19/20 and 12/25/20 (observation 4) is 1.6cm and between 12/25/20 and 12/31/20 (observation 5) is 2.3cm. However, the interferometric fringes in figure 8(a) are very noisy compared to figure 8(b). We believe the noisy fringes degrade the performance of the unwrapping algorithm significantly. Therefore, the retrieved ΔSWE is more accurate for station 5 compared to station 4. One of the main follow-ups to this study is to improve the phase unwrapping over images with low coherence.

5.1.2 Comparing Retrieved Total SWE using Sentinel-1 and SNOTEL Total SWE

In this section, we used all time series retrieved ΔSWE to calculate total SWE at each date compared to start date of our time series (12/01/2020) by

$$SWE(t_{i+1}) = \sum_{t_j=t_1}^{t_i} \Delta SWE(t_j, t_{j+1}) \tag{5}$$

where t_1 is 12/01/2020. For instance, SWE at 12/25/20 compared to 12/01/2020 is the summation of all four retrieved ΔSWE ($\Delta SWE_{12/01/20-12/07/20} + \Delta SWE_{12/07/20-12/13/20} + \Delta SWE_{12/13/20-12/19/20} + \Delta SWE_{12/19/20-12/25/20}$). As mentioned in section 5.1.1, we used ΔSWE values with temporal coherence more than 0.35 and temperature higher than $0°C$ for in situ comparison. However in this section, we used all the retrieved ΔSWE values, as the lack of ΔSWE in the time
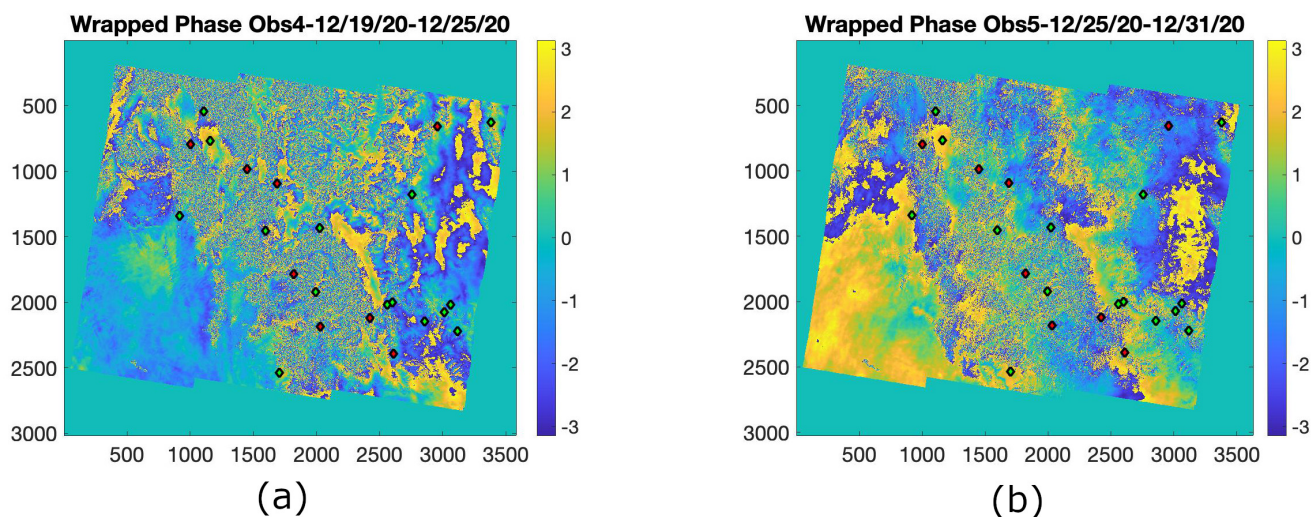

Figure 8. Sentinel-1 Wrapped Phase path:71, frame:444 between (a) 12/19/20 and 12/25/20 (Observation 4) (b) 12/25/20 and 12/31/20 (Observation 5).

series affects the total SWE. We understand that this will affect the accuracy of total SWE and we consider this in our evaluation of the results.

Figures 9 (a), (b), and (c) show the time series of total SWE for in situ stations 25, 4, and 15, respectively. The red and blue lines show the retrieved and in situ total SWE at each Sentinel-1 date acquisition compared to 12/01/2020. As seen in this figure, the time series of total retrieved SWE aligns closely with in situ values for stations 25 and 4. The error is less than 2cm in the whole time series. However, the retrieved SWE for station 15 diverges from in situ values even though it follows the same pattern. The error in total SWE estimation is about 10cm at the end of the time series. We think the main reason for divergence is the phase unwrapping error and phase ambiguity. As discussed in section 5.1.1, the noisy fringes degrade the performance of the unwrapping algorithm. A similar problem is observed in tower-based studies. The retrieval diverges from the in situ values by phase ambiguity values over large snow storms at C-band (figure 13(c) in (Ruiz et al., 2022)). However, even in these cases, the trends of SWE remain the same between retrieved and in situ values. The divergence is mainly due to phase ambiguity.

Figure 10 (a) shows the Sentinel-1 ΔSWE ambiguity versus incidence angle. The red line shows the ΔSWE ambiguity using equation 4 ($\Delta\phi = 2\pi$). The blue line shows the ΔSWE ambiguity using Leinss et al. approximation ($\Delta\phi = \kappa_i(1.59 + \theta^{2.5})\Delta SWE$) (Leinss et al., 2015). As seen in this figure, ΔSWE ambiguity is between 2 to 3.5 cm depending on the incidence angle. The relatively small ΔSWE ambiguity of Sentinel-1 makes the unwrapping challenging for snow storms. Figure 10(b) shows the temporal coherence between 02/11/21 and 02/17/21. We can see very low correlation in the snow storm regions which degrades the unwrapping process. As mentioned before, one of the main future projects of this study is to work on improving the unwrapping phase.

For each station plot in figure 9, we also report the average RSME error ($< \Delta SWEErr_{station\#} >$) and correlation ($\rho_{station\#}$) between retrieved and in situ ΔSWE, as also plotted in figure 7(b). We also report the average of temporal coherence for all the interferograms over that station ($< \rho_{temp} >$) to show how reliable the measurements at that station are. For all three sta-
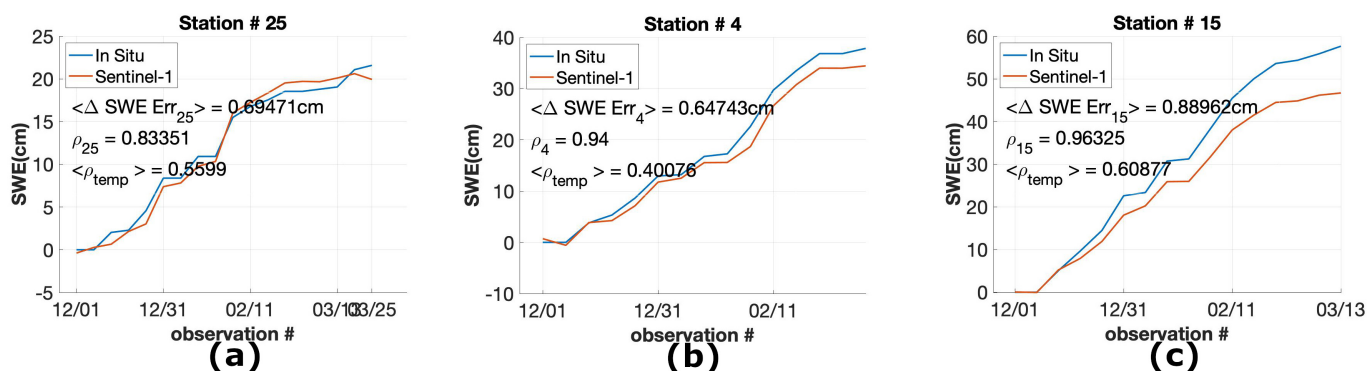

Figure 9. Time series of total in situ and retrieved SWE using Sentinel-1 interferometric phase shown by blue and red lines, respectively for stations 25 (shown in 9a), 4 (9b) and 15 (9c).

tions, the RSME error is less than 1 cm ΔSWE, the correlation between in situ and retrieved ΔSWE is greater than 0.8, and temporal coherence is greater than 0.4. The SNOTEL sites are shown by small diamonds in figure 2(b). The green small

295   diamonds have a small total SWE error, similar to stations 4 and 25. The red diamonds have a large total SWE error, similar to station 15. However, the retrieved SWE has a similar pattern as in situ SWE. Therefore, we think they have a phase unwrapping problem similar to station 15. These stations are also shown in figure 8(a). As seen in this figure, the red diamonds are mostly located in regions with noisy fringes which makes the unwrapping challenging. Among all 31 stations in the Sentinel-1 frame, 24 of them have a mean temporal coherence of more than 0.35. Hence, their Sentinel-1 data can be used for SWE estimation.

300   Among the 24 stations, 16 have a small SWE error (green diamonds) and 8 of them have a large SWE error (red diamonds).

5.2   Comparing Retrieved SWE using Sentinel-1 and LIDAR SWE

As mentioned in section 3.3, the QSI LIDAR data were collected during the SnowEx campaign. There are two LIDAR data sets collected over the Sentinel-1 path:71, frame:444 in winter 2021. The locations are shown with red rectangles in figure 2(b).

    Figure 11(a) shows the LIDAR snow depth on 3/15/21 over Banner Summit, the bigger red rectangle in figure 2(b). Similar

305   to what we did in section 5.1.2, we calculated the total SWE compared to 12/01/2020 on the closest day to LIDAR date acquisition. We used all the retrieved ΔSWE from 12/01/2020 to 03/19/2021, and calculated the total SWE on 03/19/21 using equation 5. Figure 11(b) shows the retrieved SWE on 03/19/21. Figure 11(a) and (b) have very similar patterns. The 2D-histogram of these two images is shown in figure 11(c) where x- and y-axis show the LIDAR snow depth and Sentinel-1
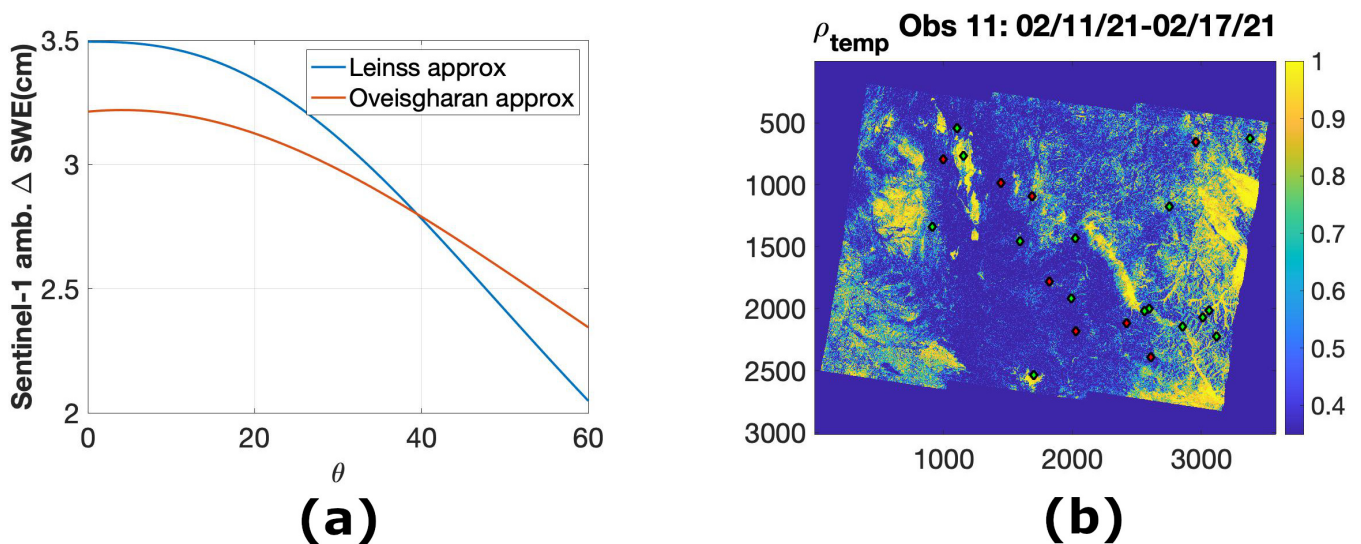

Figure 10. (a) ΔSWE ambiguity versus incidence angle using Leinss's approximation (blue line) and Oveisgharan's approximation (red line) (b) correlation for data acquired between 02/11/21 and /02/17/21 (Observation 11). Green diamonds show the location of stations with less than 5 cm total SWE error. Red diamonds show the location of stations with more than 5 cm total SWE error.

retrieved SWE, respectively. The correlation between these two data sets is 0.51. The only region with a noticeable difference

310 between the two images is the north west of the image where LIDAR shows small snow depth but retrieved data shows large SWE values. Note that the LIDAR data show the snow depth whereas Sentinel-1 retrieved data show the total SWE change during the Sentinel-1 overpasses analyzed. On the other hand, LIDAR has a much higher resolution. The high correlation (0.51) between the two data sets shows the success of this method in estimating SWE.

Figure 12(a) shows the LIDAR snow depth on 3/15/21 over Mores Creek, the smaller red rectangle in figure 2(b). We used

315 all the retrieved ΔSWE from 12/01/2020 to 03/19/2021 again, and calculated the total SWE on 03/19/21 using equation 5. Figure 12(b) shows the retrieved SWE on 03/19/21. Figure 12(a) and (b) have very similar patterns. The 2D-histogram of these two images is shown in figure 12(c) where x- and y-axis show the LIDAR snow depth and Sentinel-1 retrieved SWE,
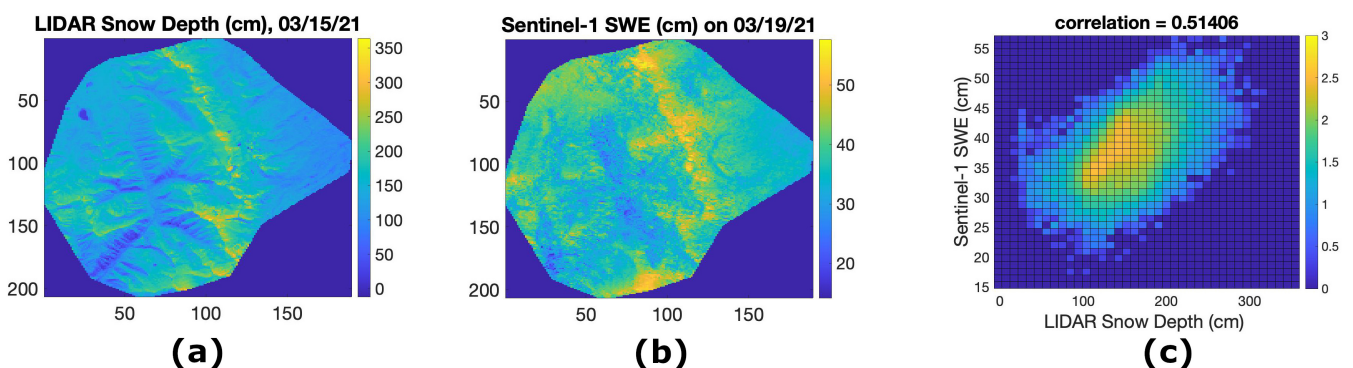

Figure 11. (a) QSI LIDAR snow depth over Banner Summit, ID on 3/15/21 (b). Retrieved total SWE using Sentinel-1 interferometric data from 12/1/20 to 3/19/21 over Banner Summit, ID. (c) 2D histogram of data in (b) versus data in (a).
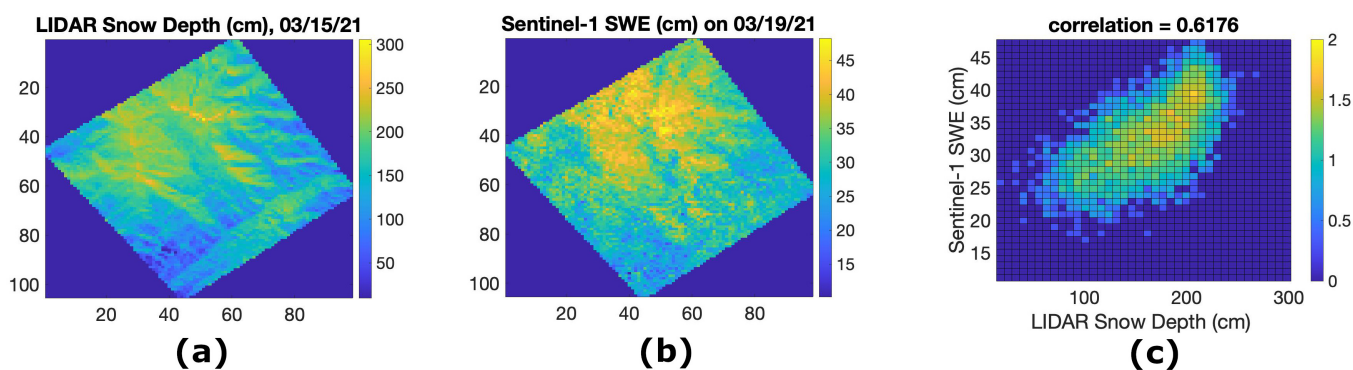

Figure 12. (a) QSI LIDAR snow depth over Mores Creek, ID on 3/15/21. (b) Retrieved total SWE using Sentinel-1 interferometric data from 12/1/20 to 3/19/21 over Mores Creek, ID. (c) 2D histogram of data in (b) versus data in (a).

15

respectively. The correlation between these two data sets is 0.62. This high correlation is one of the best validation metrics for SWE retrieval using the InSAR technique.

6 Conclusions

In this study, we used Sentinel-1 time series to retrieve ΔSWE and consequently total SWE. We chose a frame in Idaho that covers several SnowEx 2020-21 sites and 31 of SNOTEL in situ stations. LIDAR data are available for validating our results. Sentinel-1 data was collected every 6 days over this SnowEx site instead of the regular 12 days which helps a lot with temporal coherence over snowstorms. This provides a unique dense time series of spaceborne data for studying the performance of SWE retrieval using InSAR.

We showed that retrieved ΔSWE using Sentinel-1 is highly correlated (0.82) with in situ values, with an RSME of 0.76cm. The retrieved total SWE has less than 2cm RSME compared with in situ values in 16 stations. Total SWE also is highly correlated (more than 0.51) with two LIDAR images. Considering all these validations, we show for the first time that SWE retrieval using time series of InSAR spaceborne data is a very promising candidate for the future SWE mission.

The main constraints for this method are its temporal coherence, phase unwrapping, and phase ambiguity. Snow storms reduce the temporal coherence significantly. Low temporal coherence reduces the accuracy of the interferometric phase and unwrapping algorithm. Small SWE ambiguity at C-band makes the phase unwrapping more challenging. Going from C-band to lower frequencies such as L-band improves both the temporal coherence and SWE ambiguity. With the NASA-ISRO SAR mission (NISAR) launch coming next winter, we hope this dataset can be used for global SWE retrieval.

7 Acknowledgments

The Cryosphere

Discussions

References

340 Adebisi, N., Marshall, H., Vuyovich, C. M., Elder, K., Hiemstra, C., and Durand, M.: SnowEx20-21 QSI Lidar Snow Depth 0.5m UTM Grid, Version 1, https://doi.org/10.5067/VBUN16K365DG, 2022.

Baduge, A. W. A., Henschel, M. D., Hobbs, S., Buehler, S. A., Ekman, J., and Lehrbass, B.: Seasonal variation of coherence in SAR interferograms in Kiruna, Northern Sweden, Int. J. Rem. Sens., 37, 370–387, 2016.

Barnett, T., Adam, J., and Lettenmaier, D.: Potential impacts of a warming climate on water availability in snow-dominated regions, Nature,

345   438, 303–309, 2005.

Conde, V., Nico, G., Mateus, P., Catalão, J., Kontu3, A., and Gritsevich4, M.: On the estimation of temporal changes of snow water equivalent by spaceborne SAR interferometry: a new application for the Sentinel-1 mission, J. Hydrol. Hydromech., 67, 93–100, 2019.

Cui, Y., Xiong, C., Lemmetyinen, J., Shi, J., Jiang, L., Peng, B., Li, H., Zhao, T., Ji, D., and Hu, T.: Estimating Snow Water Equivalent with Backscattering at X and Ku Band on Absorption Loss, Remote Sensing, 8, 2016.

350 Dagurova, P., Chimitdorzhieva, T., Dmitriev, A., and Dobryninb, S.: Estimation of snow water equivalent from L-band radar interferometry: simulation and experiment, INTERNATIONAL JOURNAL OF REMOTE SENSING, 41, 2020.

Deeb, E. J., Forster, R. R., and Kane, D. L.: Monitoring snowpack evolution using interferometric synthetic aperture radar on the North Slope of Alaska, Int. J. Remote Sens., 32, 3985–4003, 2011.

Durand, M. and Liu, D.: The need for prior information in characterizing snow water equivalent from microwave brightness temperatures,

355   Remote Sens. Environ., 126, 248–257, 2012.

Engen, G., Guneriussen, T., and Overrein, Y.: Delta-K interferometric SAR technique for snow water equivalent (SWE) retrieval, IEEE Geosci. Remote Sens. Lett., 1, 57–61, 2004.

Eppler, J., Rabus, B., , and Morse, P.: Snow water equivalent change mapping from slope-correlated synthetic aperture radar interferometry (InSAR) phase variations, The Cryosphere,, 16, 1497–1521, 2022.

360 Gabriel, A. K., Goldstein, R. M., and Zebker, H. A.: Mapping small elevation changes over large areas: Differential radar interferometry, J. Geophys. Res., 94, 9183–9191, 1989.

Guneriussen, T., Hogda, K. A., Johnsen, H., and Lauknes, I.: InSAR for estimation of changes in snow water equivalent of dry snow, IEEE Trans. Geosci. Remote Sens., 39, 2101–2108, 2001.

H. Rott, T. N. and Scheiber, R.: Snow mass retrieval by means of SAR interferometry, Proc. 3rd Fringe Workshop Eur. Space Agency Earth

365   Observ., 2003.

Hui, L., Pengfeng, X., Xuezhi, F., Guangjun, H., and Zuo, W.: Monitoring Snow Depth And Its Change Using Repeat-Pass Interferometric SAR In Manas River Basin, IGARSS, pp. 4936–4939, 2016.

Jolivet, R., Grandin, R., Lasserre, C., Doin, M., and Peltzer, G.: Systematic InSAR tropospheric phase delay corrections from global meteorological reanalysis data, GEOPHYSICAL RESEARCH LETTERS, 38, 2011.

370 Kellndorfer, J., Cartus, O., Lavalle, M., Magnard, C., Milillo, P., Oveisgharan, S., Osmanoglu, B., Rosen, P. A., and Wegmüller, U.: Global seasonal Sentinel-1 interferometric coherence and backscatter data set, Scientific Data, 9, 2022.

Kelly, R.: The AMSR-E Snow depth algorithm: Description and initial results, J. Remote Sens. Soc. Jpn., 29, 307–317, 2009.

Kelly, R. E., Chang, A. T., Tsang, L., and Foster, J. L.: A prototype AMSR-E global snow area and snow depth algorithm, IEEE Transactions on Geoscience and Remote Sensing, 41, 230–242, 2003.

375   Larsen, Y., Malnes, E., and Engen, G.: Retrieval of snow water equivalent with envisat ASAR in a Norwegian hydropower catchment, Proc.
           IEEE Int. Geosci. Remote Sens. Symp., 8, 5444–5447, 2005.

       Lavalle, M., Simard, M., and Hensley, S.: A Temporal Decorrelation Model for Polarimetric Radar Interferometers, IEEE Transactions on
           Geoscience and Remote Sensing, 2012.

       Leinss, S., Parrella, G., and Hajnsek, I.: Snow Height Determination by Polarimetric Phase Differences in X-Band SAR Data, IEEE Journal
380   of Selected Topics in Applied Earth Observations and Remote Sensing, 7, 3794–3810, 2014.

       Leinss, S., Wiesmann, A., Lemmetyinen, J., and Hajnsek, I.: Snow Water Equivalent of Dry Snow Measured by Differential Interferometry,
           IEEE Journal of Selected Topics in Applied Earth Observations and Remote Sensing, 8, 3773–3790, 2015.

       Lemmetyinen, J., Derksen, C., Rott, H., Macelloni, G., King, J., Schneebeli, M., Wiesmann, A., Leppanen, L., Kontu, A., and Pulliainen,
           J.: Retrieval of Effective Correlation Length and Snow Water Equivalent from Radar and Passive Microwave Measurements, Remote
385   Sensing, 10, 2018.

       Lievens, H., Demuzere, M., Marshall, H.-P., Reichle, R. H., Brucker, L., Brangers, I., de Rosnay, P., Dumont, M., Girotto, M., Immerzeel,
           W. W., Jonas, T., Kim, E. J., Koch, I., Marty, C., Saloranta, T., Schöber, J., and Lannoy, G. J. D.: Snow depth variability in the Northern
           Hemisphere mountains observed from space, Nature Communications, 10, 2019.

       Lievens, H., Brangers, I., Marshall, H.-P., Jonas, T., Olefs, M., and DeLannoy, G.: Sentinel-1 snow depth retrieval at sub-kilometer resolution
390   over the European Alps, The Cryosphere, 16, 159–177, 2022.

       Liu, Y., Li, L., Yang, J., Chen, X., and Hao, J.: Estimating Snow Depth Using Multi-Source Data Fusion Based on the D-InSAR Method and
           3DVAR Fusion Algorithm, Remote Sensing, 9, 2017.

       Luzi, G., Noferini, L., Mecatti, D., Macaluso, G., Pieraccini, M., Atzeni, C., Schaffhauser, A., Fromm, R., and Nagler, T.: Using a ground-
           based SAR interferometer and a terrestrial laser scanner to monitor a snow-covered slope: Results from an experimental data collection in
395   Tyrol, IEEE Trans. Geosc. Rem. Sens., 47, 382–393, 2009.

       Marshall, H., Deeb, E., Forster, R., Vuyovich, C., Elder, K., Hiemstra, C., and Lund, J.: L-BAND INSAR DEPTH RETRIEVAL DUR-
           ING THE NASA SNOWEX 2020 CAMPAIGN: GRAND MESA, COLORADO, IEEE International Geoscience and Remote Sensing
           Symposium, pp. 625–627, 2021.

       Marshall, H.-P. and Koh, G.: FMCW radars for snow research, Cold Regions Science and Technology, 52, 118–131, 2008.

400   Mätzler, C.: Application of the interaction of Microwave with the Natural Snow Cover, Remote Sensing Reviews, 2, 259–387, 1987.

       Molan, Y. E., Kim, J.-W., Lu, Z., and Agram, P.: L-band temporal coherence assessment and modeling using amplitude and snow depth over
           interior Alaska, Remote Sens., 10, 1216–1228, 2018.

       Nagler, T., Rott, H., Scheiblauer, S., Libert, L., Mölg, N., Horn, R., Fischer, J., Keller, M., Moreira, A., and Kubanek, J.: AIRBORNE
           EXPERIMENT ON INSAR SNOW MASS RETRIEVAL IN ALPINE ENVIRONMENT, IGARSS, pp. 4549–4552, 2022.

405   Nghiem, S. V. and Tsai, W. Y.: Global snow cover monitoring with spaceborne Ku:band scatterometer, IEEE Transactions on Geoscience
           and Remote Sensing, 39, 2118–2134, 2001.

       Oveisgharan, S. and Zebker, H.: Estimating Snow Accumulation From InSAR Correlation Observations, IEEE Transactions on Geoscience
           and Remote Sensing, 45, 10–20, 2007.

       Painter, T. and et al.: The Airborne Snow Observatory: Fusion of scanning LiDAR, imaging spectrometer, and physically-based modeling
410   for mapping snow water equivalent and snow albedo, Remote Sens. Environ., 184, 139–152, 2016.

       Pulliainen, J. and Hallikainen, M.: Retrieval of regional snow water equivalent from space-borne passive microwave observations., Remote
           Sens. Environ., 75, 76–85, 2001.

Rott, H., Yueh, S. H., Cline, D. W., Duguay, C., Essery, R., Haas, C., Heliere, F., Kern, M., Macelloni, G., and Malnes, E.: Cold regions hydrology high-resolution observatory for snow and cold land processes, Proc. IEEE 2010, 98, 752–765, 2010.

415 Ruiz, J. J., Lemmetyinen, J., Kontu, A., Tarvainen, R., Vehmas, R., Pulliainen, J., and Praks, J.: Investigation of Environmental Effects on Coherence Loss in SAR Interferometry for Snow Water Equivalent Retrieval, IEEE TRANSACTIONS ON GEOSCIENCE AND REMOTE SENSING, 60, 4306 715–4306 715, 2022.

Shah, R., Xu, X., Yueh, S., Chae, C. S., Elder, K., Starr, B., and Kim, Y.: Remote Sensing of Snow Water Equivalent Using P-Band Coherent Reflection, IEEE GEOSCIENCE AND REMOTE SENSING LETTERS, 14, 309–313, 2017.

420 Takala, M., Luojus, K., Pulliainen, J., Derksen, C., and and, J. L.: Estimating northern hemisphere snow water equivalent for climate research through assimilation of space-borne radiometer data and ground-based measurements, Remote Sensing of Enviroment, 115, 3517–3529, 2011.

Ulaby, F. T. and Stiles, W. H.: The active and passive microwave response to snow parameters: 2. Water equivalent of dry snow., J. Geophys. Res. Oceans (1978–2012), 85, 1045–1049, 1980.

425 Yueh, S. H., Xu, X., Shah, R., Kim, Y., Garrison, J. L., Komanduru, A., and Elder, K.: Remote Sensing of Snow Water Equivalent Using Coherent Reflection From Satellite Signals of Opportunity: Theoretical Modeling, IEEE Journal of Selected Topics in Applied Earth Observations and Remote Sensing, 10, 5529–5540, 2017.

Yueh, S. H., Shah, R., Xu, X., Stiles, B., and Bosch-Lluis, X.: A Satellite Synthetic Aperture Radar Concept Using P-Band Signals of Opportunity, IEEE JOURNAL OF SELECTED TOPICS IN APPLIED EARTH OBSERVATIONS AND REMOTE SENSING, 14, 2796–2816, 2021.

430 Yunjun, Z., Fattahi, H., and Amelung, F.: Small baseline InSAR time series analysis: Unwrapping error correction and noise reduction, Computer and Geoscience, 133, 5529–5540, 2019.

Zebker, H. A. and Villasenor, J.: Decorrelation in Interferometric Radar Echoes, IEEE TRANSACTIONS ON GEOSCIENCE AND RE-MOTE SENSING, 30, 950–959, 1992.

435 Zebker, H. A., Rosen, P. A., Goldstein, R., Gabriel, A., and L.Werner, C.: On the derivation of coseismic displacement fields using differential radar interferometry: The Landers earthquake, J. Geophys. Res. Solid Earth, 99, 19 617–19 634, 1994.